A parsec-scale cm-to-sub-mm SED study of the compact radio jet components in NGC 1068

Downloaded from: https://research.chalmers.se, 2026-11-10 06:27 UTC

Citation for the original published paper (version of record):
Mutie, I., Del Palacio, S., Williams-Baldwin, D. et al (2026). A parsec-scale cm-to-sub-mm SED study of the compact radio jet components in NGC 1068. Monthly Notices of the Royal Astronomical Society, 552(1). http://dx.doi.org/10.1093/mnras/stag1693

N.B. When citing this work, cite the original published paper.

research.chalmers.se offers the possibility of retrieving research publications produced at Chalmers University of Technology. It covers all kind of research output: articles, dissertations, conference papers, reports etc. since 2004. research.chalmers.se is administrated and maintained by Chalmers Library

(article starts on next page)

Monthly Notices of the ROYAL ASTRONOMICAL SOCIETY

MNRAS **552,** 1–9 (2026)
Advance Access publication 2026 September 16

https://doi.org/10.1093/mnras/stag1693

A parsec-scale cm-to-sub-mm SED study of the compact radio jet components in NGC 1068

Isaac M. Mutie [1,2★] Santiago del Palacio [3] David Williams-Baldwin [2] Robert J. Beswick,[2] Susanne E. Aalto,[3] Violette C. M. Impellizzeri,[4,5] John S. Gallagher[6,7] and Jack F. Gallimore[8]

[1]*Department of Astronomy and Space Science, Technical University of Kenya, P.O. Box 52428-00200, Nairobi, Kenya*
[2]*Jodrell Bank Centre for Astrophysics, School of Physics and Astronomy, The University of Manchester, Manchester M13 9PL, UK*
[3]*Department of Space, Earth and Environment, Chalmers University of Technology, SE-412 96 Göteborg, Sweden*
[4]*Leiden Observatory, Leiden University, PO Box 9513, NL-2300 RA Leiden, the Netherlands*
[5]*ASTRON, Netherlands Institute for Radio Astronomy, NL-7991 PD Dwingeloo, the Netherlands*
[6]*Department of Physics and Astronomy, Macalester College, 1600 Grand Ave, St. Paul, MN 55105, USA*
[7]*Department of Astronomy, University of Wisconsin–Madison, 475 North Charter St, Madison, WI 53706, USA*
[8]*Department of Physics and Astronomy, Bucknell University, Lewisburg, PA 17837, USA*

Accepted 2026 September 4. Received 2026 September 3; in original form 2026 May 13

ABSTRACT

We present parsec-scale cm-to-sub-mm spectral energy distributions (SEDs) of the compact radio-jet components NE, C, S2, and S3 in the Seyfert 2 galaxy NGC 1068. Matched-*uv e*-MERLIN, VLA, and ALMA imaging spans 4.5–706 GHz at a common 0.06-arcsec resolution and 15–3300 kλ *uv*-coverage. Spatial-blending tests show weak inter-component covariance, less than 1 per cent direct neighbour-induced flux transfer, and a maximum S2 perturbation of 8.4 per cent across the 18.9–22.9-GHz turnover region, corresponding to $|\Delta\nu_{\rm cl}| \lesssim 1.6$ GHz or $|\Delta f_{\rm cov}| \lesssim 0.06$. Bayesian MCMC modelling with synchrotron emission, free–free emission, and free–free absorption yields steep intrinsic synchrotron indices, $\alpha_{\rm sy} \simeq -0.9$ to -1.7. The cut-off is lowest in C, $\nu_{\rm c} = 420^{+146}_{-103}$ GHz. NE and S3 have measured cut-offs of 634^{+244}_{-225} and 598^{+264}_{-231} GHz, respectively, whereas S2 yields only the lower limit $\nu_{\rm c} > 418$ GHz. A partial-covering absorber is favoured for all four components (ΔAIC = 6.6–30.1; ΔBIC = 4.3–28.0). NE, C, and S3 have comparable clump-opacity scales, $\nu_{\rm cl} \simeq 11$–12 GHz, and covering factors, $f_{\rm cov} \simeq 0.43$–0.53, with C additionally requiring diffuse absorption. S2 is the clear exception, with $\nu_{\rm cl} = 26.0^{+1.8}_{-2.1}$ GHz and $f_{\rm cov} = 0.83^{+0.05}_{-0.07}$; its opacity scale differs from those of the other components by approximately 4.8–5.6σ. The results support a sightline-dependent ionized medium in which S2 intersects the densest and most strongly covering absorber, plausibly near the torus–inner-narrow-line region interface. No off-nuclear component requires a significant mm–sub-mm excess above the synchrotron model.

Key words: interstellar medium – galaxies: individual: NGC1068 – galaxies: jets – radio continuum.

1 INTRODUCTION

The nearby (∼14.4 Mpc) Seyfert 2 galaxy NGC 1068 is a benchmark system for investigating the nuclear environments of obscured active galactic nuclei (AGNs; J. F. Gallimore et al. 1996a; S. García-Burillo et al. 2016, 2019; C. M. V. Impellizzeri et al. 2019). Its proximity and complex circumnuclear medium make it particularly well suited for studying the interaction between compact radio jets and the surrounding interstellar medium (ISM; S. Viti et al. 2014; S. García-Burillo et al. 2016; C. M. V. Impellizzeri et al. 2019; I. M. Mutie et al. 2024). Very-long-baseline radio interferometry (VLBI) observations resolve the AGN (S1) and several compact neighbouring components into an elongated, pc-scale jet structure oriented nearly perpendicular to the kpc-scale radio outflow (T. W. B. Muxlow et al. 1996; J. F. Gallimore et al. 1996a; J. F. Gallimore, S. A. Baum & C. P. O'Dea 2004; I. M. Mutie et al. 2024).

The jet components reside close to the AGN and are consistent with classical synchrotron emitters (T. W. B. Muxlow et al. 1996; J. F. Gallimore et al. 1996a; I. M. Mutie et al. 2024). Their flux densities and resolved sizes imply low brightness temperatures, making synchrotron self-absorption negligible (J. F. Gallimore et al. 1996a). Consequently, any low-frequency spectral flattening is more plausibly attributed to free–free absorption (FFA) by ionized gas along the line of sight. Inhomogeneous, clumpy FFA is expected to partially absorb intrinsically steep synchrotron spectra, producing flattened or inverted spectra below a characteristic turnover frequency (M. S. Clemens et al. 2010; B. C. Lacki 2013a; J. E. Conway, M. Elitzur & R. Parra 2018; I. M. Mutie et al. 2025). Such a scenario has been successfully applied to the AGN where a population of dense ionized clumps partially covers the source, resulting in the observed cm-wave spectral be-

★ E-mail: mumoisaac@gmail.com

© The Author(s) 2026.
Published by Oxford University Press on behalf of Royal Astronomical Society. This is an Open Access article distributed under the terms of the Creative Commons Attribution License (https://creativecommons.org/licenses/by/4.0/), which permits unrestricted reuse, distribution, and reproduction in any medium, provided the original work is properly cited.

Downloaded from academic.oup.com/mnras/article/552/1/stag1693/8802537 by guest on 28 September 2026

Table 1. Continuum measurements used to construct and fit the compact-component SEDs. The NE, C, S2, and S3 columns give integrated flux densities in mJy; the final column gives the image rms in μJy beam^{-1}. *Note:* Detected component flux densities were measured with IMFIT from images matched to a common 0.06 arcsec restoring beam and 15–3300 kλ *uv*-coverage. The quoted measurement uncertainties are statistical fitting uncertainties; absolute-flux calibration uncertainties were included separately in the SED modelling. The 1.4 and 15 GHz values are lower-resolution upper limits. For ALMA non-detections, the adopted 3σ integrated-flux upper limits differ from the single-beam rms values in the final column. The observations, dates, and project identifiers are listed in table 1 of I. M. Mutie et al. (2025).

Frequency (GHz)	Integrated flux density (mJy) NE	C	S2	S3	rms (μJy beam^{-1})
1.4	<283.0	<42.3	<20.0	<69.7	<330
4.8	62.3 ± 0.3	80.0 ± 0.27	27.2 ± 0.3	14.8 ± 0.3	43
5.3	54.9 ± 0.3	70.0 ± 0.23	18.5 ± 0.3	12.4 ± 0.3	27
6.3	35.9 ± 0.2	45.3 ± 0.21	15.2 ± 0.2	6.1 ± 0.2	31
6.8	34.0 ± 0.2	41.4 ± 0.22	16.6 ± 0.2	7.1 ± 0.2	31
7.3	23.0 ± 0.2	38.5 ± 0.41	11.6 ± 0.2	5.0 ± 0.2	31
9.5	32.9 ± 0.1	48.8 ± 0.1	7.4 ± 0.1	8.5 ± 0.1	37
10.5	30.7 ± 0.1	47.9 ± 0.1	7.3 ± 0.1	9.1 ± 0.1	37
11.5	25.7 ± 0.1	40.8 ± 0.1	5.8 ± 0.1	7.0 ± 0.1	37
15	<54	<75.0	–	–	–
18.9	15.5 ± 0.1	28.2 ± 0.1	5.3 ± 0.1	4.3 ± 0.1	23
19.4	15.2 ± 0.1	27.5 ± 0.1	5.1 ± 0.1	4.1 ± 0.1	23
19.9	14.8 ± 0.1	26.9 ± 0.1	5.0 ± 0.1	4.0 ± 0.1	37
21.9	13.3 ± 0.1	25.2 ± 0.1	4.6 ± 0.1	3.4 ± 0.1	53
22.3	13.0 ± 0.1	25.2 ± 0.1	4.2 ± 0.1	3.5 ± 0.1	54
22.9	12.5 ± 0.1	24.7 ± 0.1	4.3 ± 0.1	3.4 ± 0.1	52
94	2.3 ± 0.1	5.6 ± 0.1	1.3 ± 0.1	1.31 ± 0.04	24
105	1.9 ± 0.1	5.4 ± 0.1	0.9 ± 0.1	0.82 ± 0.03	24
249	0.6 ± 0.1	2.5 ± 0.1	0.4 ± 0.1	0.4 ± 0.1	24
357	<0.6	1.1 ± 0.15	<0.9	<0.7	87
477	<0.6	<0.6	<0.6	<0.6	170
706	<0.3	<0.3	<0.3	<0.3	75

haviour (I. M. Mutie et al. 2025). Given the dense and asymmetric circumnuclear medium in NGC 1068, similar absorption effects may also influence the observed spectra of the compact jet components, particularly on the south-western side where the jet appears disrupted and faint.

Broad-band spectral energy distributions (SEDs) extending from cm to sub-mm wavelengths provide a powerful diagnostic of the competing emission and absorption processes in these compact regions. While the jet components are expected to be dominated by synchrotron emission, deviations at high frequencies could signal additional contributions from free–free (FF) emission, dust, or particle re-acceleration associated with shocks or embedded star-forming clumps (E. Järvelä, M. Berton & L. Crepaldi 2021). High-frequency ALMA observations up to ∼706 GHz offer the opportunity to identify the transition from non-thermal to thermal emission and to isolate the intrinsic synchrotron spectra of the jets.

In this work, we focus on the compact off-nuclear jet components NE, C, S2, and S3 (I. M. Mutie et al. 2025). The AGN core, S1, was analysed separately in I. M. Mutie et al. (2025) and is therefore excluded from the SED fitting presented here. We test whether the broad-band spectra of the off-nuclear components can be adequately described by synchrotron emission viewed through a homogeneous, diffuse ionized screen, or whether the data statistically favour an additional partial-covering FF absorber. We subsequently examine whether the inferred absorption properties differ significantly among the individual components and assess the robustness of these results to spatial blending and variability arising from the non-simultaneous observations.

A central feature of our analysis is the use of images matched in both angular resolution and (*uv*)-coverage. This procedure mitigates a major source of bias in multifrequency studies, in which apparent spectral differences may arise from variations in angular resolution and sensitivity to different spatial scales between data sets. It therefore enables a consistent component-by-component comparison of the broad-band SEDs. To our knowledge, this is the first time that such an approach has been applied to the SEDs of the compact jet components in NGC 1068.

2 OBSERVATIONS, DATA REDUCTION, AND IMAGING

We combine multi-epoch *e*-MERLIN observations at 1.25–1.76 and 4.5–7.5 GHz with matched-resolution VLA data at 8–12 and 18.5–23.5 GHz and ALMA observations spanning 93–706 GHz. Full details of the data sets, observing dates, project identifiers, calibration, and imaging are given in table 1 of I. M. Mutie et al. (2025).

The data were calibrated using standard CASA-based pipelines (J. P. McMullin et al. 2007), followed by targeted self-calibration, and imaged with a common 15–3300 kλ *uv*-range and 0.06 arcsec restoring beam. This corresponds to ∼4 pc at the distance of NGC 1068, allowing the principal compact jet components to be separated, although not their sub-pc internal structures.

Downloaded from academic.oup.com/mnras/article/552/1/stag1693/8802537 by guest on 28 September 2026

Table 2. Spatial-blending diagnostics for the compact jet components across the matched-resolution 4.8–22.9-GHz images. Separations are given in arcseconds and in units of the common 60-mas restoring-beam FWHM. Here, $|\rho|$ is the maximum absolute fitted-amplitude correlation, $\Delta S_{\pm 20\ \mathrm{per\ cent}}$ is the largest target-flux change after perturbing the neighbouring amplitude by ±20 per cent, and ϵ_{95} is the largest 95th-percentile error from the injection recovery trials. Component S1 is included only as a possible contaminating neighbour.

Target	Nearest neighbour	Separation (arcsec/beams)	Maximum $\lvert\rho\rvert$	$\Delta S_{\pm 20\ \mathrm{per\ cent}}$ (per cent)	ϵ_{95} (per cent)
NE	C	0.352/5.86	0.020	0.65	1.29
C	S1	0.308/5.14	0.113	0.98	1.72
S2	S1	0.119/1.99	0.032	0.92	3.07

Integrated component flux densities were measured from the matched images using IMFIT and are listed in Table 1. Non-detections were assigned 3σ integrated-flux upper limits, while the lower-resolution 1.4 and 15 GHz measurements were treated as conservative upper limits. Cross-instrument calibration uncertainties were included separately in the SED modelling following I. M. Mutie et al. (2025).

2.1 Assessment of inter-component flux mixing

To quantify covariance between adjacent components, we performed image-plane deblending on all matched-resolution images from 4.8 to 22.9 GHz. Reference positions for NE, C, S1, and S2 were taken from the high signal-to-noise 4.8-GHz image, with S1 included only as a possible contaminating neighbour. The components were fitted simultaneously using beam-convolved Gaussian templates and a planar background, with an optional broad C–S1 bridge component used to test sensitivity to diffuse emission.

Transverse-averaged profiles were extracted along the NE, C, S1, S2 jet axis through a 0.060 arcsec-wide strip. Supplementary Fig. S1 shows the 4.8, 10.5, and 22.3 GHz maps and their profile decompositions. These fits were used only to assess covariance and fitting sensitivity and do not replace the IMFIT flux densities in Table 1.

Robustness was tested by shifting each centroid by ±10 mas, with an additional conservative 30-mas test for the Very Large Array (VLA) X-band images, and by fixing neighbouring amplitudes at ±20 per cent of their joint-fitting values while refitting the target component. We also derived the amplitude covariance matrix and performed 150 injection recovery trials per frequency using the measured beam and correlated image noise. The covariance, perturbation, and injection recovery results are summarized in Table 2.

3 SPECTRAL ENERGY DISTRIBUTION MODELLING

The SED modelling follows the framework used by I. M. Mutie et al. (2025). We model the continuum flux densities measured at uniform angular resolution and matched *uv*-coverage, while treating the lower-resolution measurements as conservative upper limits. Each component is described using the same intrinsic emission prescription, but two alternative FF absorption geometries are fitted and compared. The partial-covering clumpy absorber is therefore not assumed a priori; its inclusion is tested quantitatively against a simpler diffuse-only model before any physical interpretation is made.

The model parameters are inferred using the framework of S. del Palacio et al. (2025), which performs Bayesian inference with the EMCEE Markov chain Monte Carlo sampler (MCMC; D. Foreman-Mackey et al. 2013), implemented through BILBY (G. Ashton et al. 2019). Uniform priors are adopted over broad, physically motivated parameter ranges, and the spectral fits are centred at a fiducial frequency of $\nu_0 = 100$ GHz. The full one- and two-dimensional posterior distributions, including the principal parameter covariances, are shown in Supplementary Figs S2 to S5 for NE, C, S2, and S3, respectively.

3.1 Intrinsic emission components

The intrinsic continuum is represented by synchrotron emission from relativistic electrons, optically thin FF emission from ionized gas, and a possible thermal-dust contribution. The synchrotron component, including the high-frequency exponential cut-off, is written as

$$S_{\mathrm{sy,int}}(\nu) = A_{\mathrm{sy}} \left(\frac{\nu}{\nu_0}\right)^{\alpha_{\mathrm{sy}}} \exp\left(-\frac{\nu}{\nu_{\mathrm{c}}}\right), \tag{1}$$

where A_{sy} is the synchrotron normalization, $\alpha_{\mathrm{sy}} \leq -0.5$ is the intrinsic synchrotron spectral index, and ν_{c} is the high-frequency exponential cut-off. This same $S_{\mathrm{sy,int}}(\nu)$ is the intrinsic synchrotron spectrum used in the diffuse and partial-covering absorption expressions below.

The optically thin FF component is

$$S_{\mathrm{ff}}(\nu) = A_{\mathrm{ff}} \left(\frac{\nu}{\nu_0}\right)^{-0.1}, \tag{2}$$

where A_{ff} is its normalization. The low-frequency optically thick FF emission regime is not modelled separately because the observed low-frequency SEDs are dominated by synchrotron emission and absorption, and an additional turnover would be poorly constrained by the available data. The possible thermal-dust contribution is represented by the modified-blackbody prescription used by I. M. Mutie et al. (2025),

$$S_{\mathrm{d}}(\nu) = A_{\mathrm{d}} \left(\frac{\nu}{\nu_0}\right)^{2} \left[1 - \exp\left(-\tau_{\mathrm{d}}(\nu)\right)\right], \tag{3}$$

where

$$\tau_{\mathrm{d}}(\nu) = \left(\frac{\nu}{\nu_{\tau=1}}\right)^{\beta}. \tag{4}$$

We fix $\beta = 2$ and $\nu_{\tau=1} = 800$ GHz and fit only the normalization A_{d}. The available data yield only upper limits on A_{d} for all four components.

3.2 Diffuse-only absorption model

The baseline absorption model places the intrinsic synchrotron emission behind a homogeneous diffuse ionized screen,

$$S^{\mathrm{diff}}_{\mathrm{sy,abs}}(\nu) = S_{\mathrm{sy,int}}(\nu) \exp[-\tau_{\mathrm{diff}}(\nu)], \tag{5}$$

where $S_{\mathrm{sy,int}}(\nu)$ is given explicitly by equation (1). The diffuse FF optical depth is

$$\tau_{\mathrm{diff}}(\nu) = \left(\frac{\nu}{\nu_{\mathrm{diff}}}\right)^{-2.1}, \tag{6}$$

Downloaded from academic.oup.com/mnras/article/552/1/stag1693/8802537 by guest on 28 September 2026

where $\nu_{\rm diff}$ is the frequency at which $\tau_{\rm diff} = 1$. This model provides the minimal reference against which the additional partial-covering component is tested.

3.3 Partial-covering clumpy absorption model

The alternative model allows a fraction of the intrinsic synchrotron source to be covered by denser ionized structures in addition to the diffuse screen (e.g. B. C. Lacki 2013b; J. E. Conway et al. 2018; N. Ramírez-Olivencia et al. 2022). Its absorbed synchrotron spectrum is

$$S^{\rm cl}_{\rm sy,abs}(\nu) = S_{\rm sy,int}(\nu)\left[1 - f_{\rm cov}\left(1 - {\rm e}^{-\tau_{\rm cl}(\nu)}\right)\right]{\rm e}^{-\tau_{\rm diff}(\nu)}, \quad (7)$$

where $S_{\rm sy,int}(\nu)$ is the cut-off synchrotron spectrum defined by equation (1) and $f_{\rm cov}$ is the fraction of the synchrotron emission covered by the clumpy absorber. The clumpy-screen optical depth is

$$\tau_{\rm cl}(\nu) = \left(\frac{\nu}{\nu_{\rm cl}}\right)^{-2.1}, \quad (8)$$

where $\nu_{\rm cl}$ is the frequency at which the corresponding optical depth equals unity, while $\tau_{\rm diff}(\nu)$ is defined in Section 3.2 and is common to both absorption models.

Relative to the diffuse-only model, the clumpy model adds the two parameters $f_{\rm cov}$ and $\nu_{\rm cl}$. The shared intrinsic-emission and diffuse-absorption parameters are treated consistently in both fits.

3.4 Statistical model comparison

The necessity of the partial-covering component is assessed before interpreting its fitted parameters. For each component, we compare the diffuse-only and clumpy-absorber fits using the Akaike and Bayesian Information Criteria,

$$\mathrm{AIC} = 2k - 2\ln\widehat{\mathcal{L}}, \qquad \mathrm{BIC} = k\ln N_{\rm data} - 2\ln\widehat{\mathcal{L}}, \quad (9)$$

where k is the number of fitted parameters, $N_{\rm data}$ is the number of measurements entering the fit, and $\widehat{\mathcal{L}}$ is the maximum likelihood. We define

$$\Delta\mathrm{AIC}{=}\mathrm{AIC}_{\rm diffuse} - \mathrm{AIC}_{\rm clumpy}, \quad \Delta\mathrm{BIC}{=}\mathrm{BIC}_{\rm diffuse} - \mathrm{BIC}_{\rm clumpy}. \quad (10)$$

Positive values favour the clumpy model after penalizing its additional parameters. The quantitative comparison is presented first in Section 4.1; only thereafter are $f_{\rm cov}$, $\nu_{\rm cl}$, and their physical implications discussed. This ordering avoids assuming the clumpy interpretation in advance of the statistical evidence.

4 RESULTS

Fig.1 shows the locations of NE, C, S2, and S3 relative to the AGN component S1 while Fig. 2 presents the matched-resolution cm-to-sub-mm SEDs of the four off-nuclear components analysed here. These are constructed from matched-resolution ($\simeq$ 0.06 arcsec) and matched-uv (15–3300 kλ) data spanning 4.5–706 GHz. The component flux densities and upper limits used in these SEDs are listed in Table 1, while the best-fitting parameters are given in Table 3. The complete posterior distributions for NE, C, S2, and S3 are shown in Supplementary Figs S2 to S5, respectively.

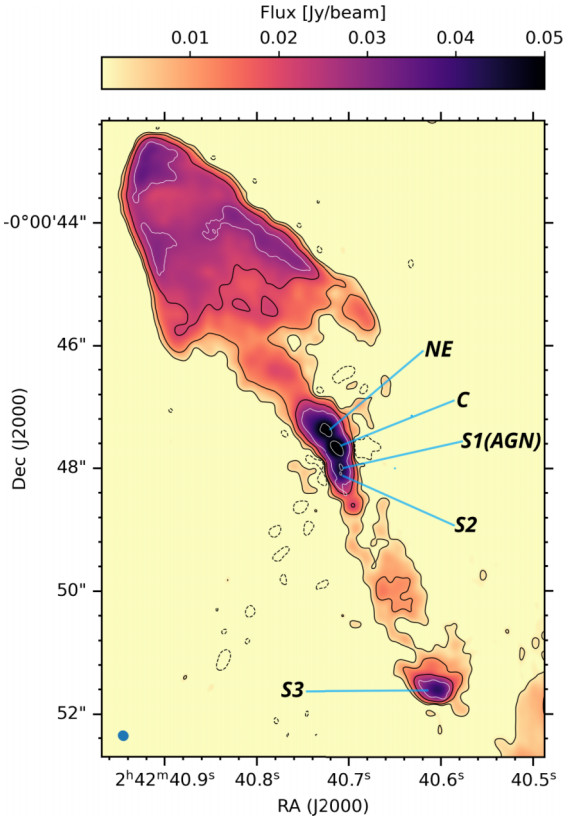

Figure 1. Composite *e*-MERLIN + VLA 4–12-GHz image of the inner radio jet in NGC 1068, showing the AGN component S1 and the compact off-nuclear components NE, C, S2, and S3. The image is reproduced in compact form from Mutie 2024; S1 is included here for morphological context and as the nearest potential contaminant of S2, but is not included in the off-nuclear SED fitting. This overview image is not used for the matched-resolution flux-density measurements.

4.1 Quantitative requirement for the clumpy absorber

Before interpreting the absorption parameters, we first test whether the additional partial-covering component is warranted by the data. Relative to the diffuse-only model, the clumpy model gives (ΔAIC, ΔBIC) = (8.3, 6.1) for NE, (6.6, 4.3) for C, (30.1, 28.0) for S2, and (6.9, 4.7) for S3. Both criteria are positive for every component even though the clumpy model contains two additional parameters. The preference is decisive for S2, strong for NE, and moderate to strong for C and S3, depending on the criterion adopted. We therefore use the clumpy-absorber fits for the parameter summaries below and defer their physical interpretation to Section 5.2.

4.2 Robustness to spatial blending

Supplementary Fig. S1 shows the matched-resolution 4.8, 10.5, and 22.3 GHz images and corresponding transverse-averaged profiles along the NE, C, S1, S2 jet axis. The 60 mas coloured intervals mark one common restoring-beam full width at half-maximum (FWHM), while the profile decomposition includes the compact components and the broad C to S1 bridge. S1 is included only as the nearest potential contaminant of S2 and is not fitted in the off-nuclear SED analysis.

Downloaded from academic.oup.com/mnras/article/552/1/stag1693/8802537 by guest on 28 September 2026

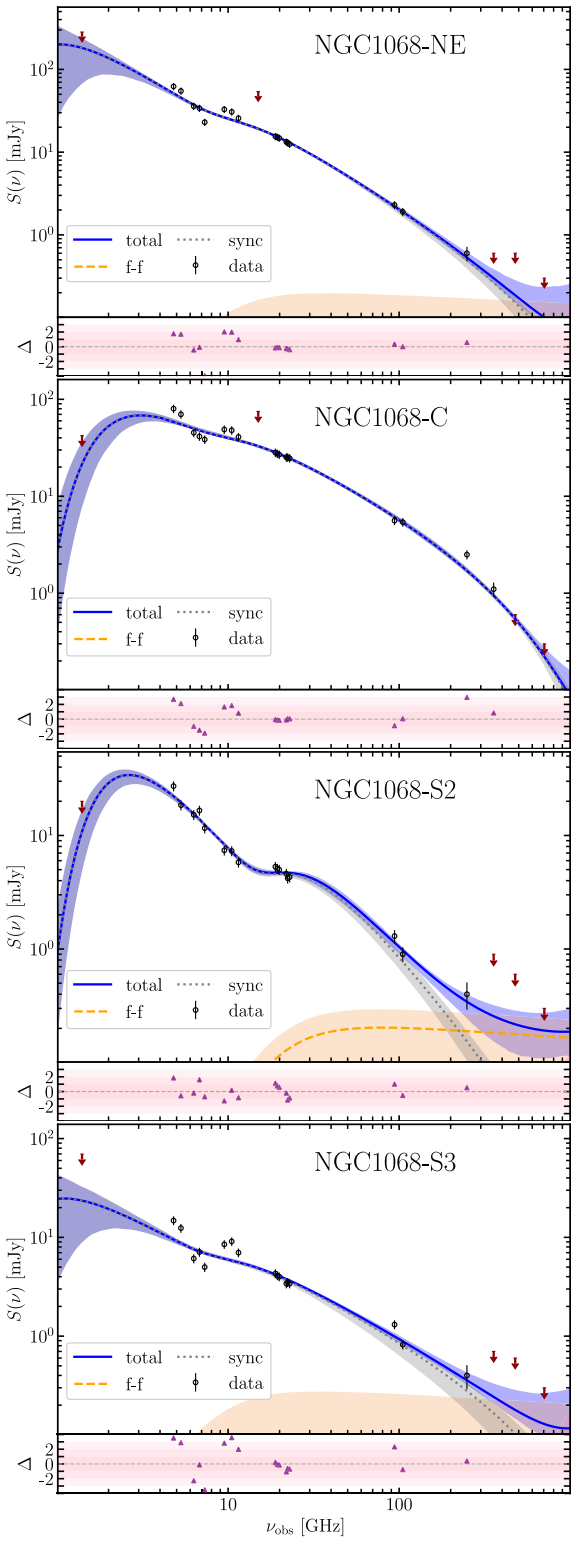

Figure 2. Matched-resolution cm-to-sub-mm SEDs of the compact jet components NE, C, S2, and S3. Circles are detections and arrows are upper limits. The solid blue curve is the posterior median total model, the grey dotted curve is the synchrotron contribution, and the orange dashed curve is the free–free contribution. The shaded regions show the 16th–84th percentile interval of the corresponding model component. The thermal-dust contribution is included in the fitting but is not shown because its upper limit is below the scale of the plots. The lower panels show the normalized residuals, $\Delta = (S_{\rm obs} - S_{\rm model})/\sigma_{\rm obs}$.

The centroid separations are 0.352 arcsec for NE to C, 0.308 arcsec for C to S1, and 0.119 arcsec for S1 to S2, corresponding to 5.86, 5.14, and 1.99 common beamwidths, respectively. NE and C are therefore well separated, while the closest pair, S1 to S2, remains resolved into distinct contributions, including at 22.3 GHz. Quantitative contamination limits are derived from the covariance and perturbation tests rather than from separation alone.

Across fits with and without the broad bridge component, the maximum absolute amplitude correlations are $|\rho| = 0.020, 0.113$, and 0.032 for NE to C, C to S1, and S1 to S2, respectively. Fixing the nearest-neighbour amplitude 20 per cent above or below its best-fitting value changes the NE, C, and S2 fluxes by at most 0.65 per cent, 0.98 per cent, and 0.92 per cent. Injection–recovery trials give median biases below 0.32 per cent and maximum 95th-percentile errors of 1.29 per cent, 1.72 per cent, and 3.07 per cent, respectively.

Centroid placement produces the larger uncertainty. A 10-mas displacement changes the recovered fluxes by at most 7.7 per cent for NE, 6.8 per cent for C, and 13.0 per cent for S2; around the S2 turnover, the maximum change is 8.4 per cent. The deliberately conservative 30-mas X-band displacement changes S2 by 24–29 per cent, but represents a half-beam stress test rather than a realistic registration uncertainty.

The resulting effect on the absorption parameters can be bounded from the partial-covering model. At $\nu = \nu_{\rm cl}$, define

$$A_{\rm cl} = 1 - f_{\rm cov}(1 - {\rm e}^{-1}). \tag{11}$$

For a small fractional flux bias ϵ, with all other parameters fixed,

$$\left|\frac{\Delta\nu_{\rm cl}}{\nu_{\rm cl}}\right| \simeq \frac{A_{\rm cl}{\rm e}}{2.1 f_{\rm cov}}|\epsilon|, \qquad |\Delta f_{\rm cov}| \simeq \frac{A_{\rm cl}}{1-{\rm e}^{-1}}|\epsilon|. \tag{12}$$

For S2, the conservative 8.4 per cent turnover-band perturbation implies $|\Delta\nu_{\rm cl}| \lesssim 1.6$ GHz or $|\Delta f_{\rm cov}| \lesssim 0.06$. These shifts are comparable to the statistical uncertainties but cannot reduce $\nu_{\rm cl} = 26.0^{+1.8}_{-2.1}$ GHz to the $\simeq$ 11–12 GHz values of NE, C, and S3. Spatial blending may therefore broaden precise parameter comparisons, but it cannot account for the unusually strong absorption inferred for S2.

4.3 Best-fitting component SEDs

Component NE has an intrinsic synchrotron index $\alpha_{\rm sy} = -1.27^{+0.09}_{-0.09}$, a clump optical-depth scale $\nu_{\rm cl} = 12.1^{+1.5}_{-1.4}$ GHz, and a covering factor $f_{\rm cov} = 0.53^{+0.08}_{-0.09}$. Its diffuse opacity is not significantly constrained, with $\nu_{\rm diff} < 1.59$ GHz, and its synchrotron cut-off is $\nu_{\rm c} = 634^{+244}_{-225}$ GHz. Component C has $\alpha_{\rm sy} = -0.94^{+0.13}_{-0.10}$, $\nu_{\rm cl} = 11.6^{+2.1}_{-2.2}$ GHz, $f_{\rm cov} = 0.43^{+0.10}_{-0.14}$, and a measured diffuse component $\nu_{\rm diff} = 2.11^{+0.42}_{-0.25}$ GHz. Its cut-off is lower, $\nu_{\rm c} = 420^{+146}_{-103}$ GHz.

Component S2 has the steepest intrinsic spectrum, $\alpha_{\rm sy} = -1.67^{+0.14}_{-0.14}$, and the largest fitted absorption parameters, with $\nu_{\rm cl} = 26.0^{+1.8}_{-2.1}$ GHz, $f_{\rm cov} = 0.83^{+0.05}_{-0.07}$, and $\nu_{\rm diff} = 2.37^{+0.32}_{-0.22}$ GHz. Its synchrotron cut-off is constrained to $\nu_{\rm c} > 418$ GHz. Component S3 has $\alpha_{\rm sy} = -0.95^{+0.13}_{-0.17}$, $\nu_{\rm cl} = 11.0^{+1.7}_{-1.7}$ GHz, $f_{\rm cov} = 0.46^{+0.12}_{-0.14}$, $\nu_{\rm diff} < 1.56$ GHz, and $\nu_{\rm c} = 598^{+264}_{-231}$ GHz.

To quantify the extent to which S2 differs from the other components, we define a conservative Gaussian-equivalent tension statistic using the one-sided uncertainties directed towards

Downloaded from academic.oup.com/mnras/article/552/1/stag1693/8802537 by guest on 28 September 2026

Table 3. Best-fitting SED model parameters for the compact jet components in NGC 1068, derived from the posterior distributions obtained with MCMC sampling. Uncertainties correspond to the 16th–84th percentile intervals. For parameters reaching a hard prior boundary, only the corresponding upper or lower limit is reported. The quantities ΔAIC and ΔBIC compare the model containing a partial-covering clumpy absorber with the diffuse-only model; positive values favour the clumpy-absorber model (Section 3.3). Full posterior distributions and parameter covariances are shown in Supplementary Figs S2 to S5.

Component	α_{sy}	A_{sy}	A_{ff}	A_d	ν_c (GHz)	ν_{cl} (GHz)	f_{cov}	ν_{diff} (GHz)	ΔAIC	ΔBIC
NE	$-1.27^{+0.09}_{-0.09}$	$1.64^{+0.05}_{-0.05}$	< -0.6	< -1.5	634^{+244}_{-225}	$12.1^{+1.5}_{-1.4}$	$0.53^{+0.08}_{-0.09}$	< 1.59	8.3	6.1
C	$-0.94^{+0.13}_{-0.10}$	$1.80^{+0.06}_{-0.07}$	< -0.5	< -1.5	420^{+146}_{-103}	$11.6^{+2.1}_{-2.2}$	$0.43^{+0.10}_{-0.14}$	$2.11^{+0.42}_{-0.25}$	6.6	4.3
S2	$-1.67^{+0.14}_{-0.14}$	$1.67^{+0.13}_{-0.14}$	$-0.58^{+0.16}_{-0.57}$	< -2.06	> 418	$26.0^{+1.8}_{-2.1}$	$0.83^{+0.05}_{-0.07}$	$2.37^{+0.32}_{-0.22}$	30.1	28.0
S3	$-0.95^{+0.13}_{-0.17}$	$0.95^{+0.07}_{-0.07}$	$-0.97^{+0.48}_{-0.94}$	< -1.5	598^{+264}_{-231}	$11.0^{+1.7}_{-1.7}$	$0.46^{+0.12}_{-0.14}$	< 1.56	6.9	4.7

overlap,

$$Z_i = \frac{\nu_{cl,S2} - \nu_{cl,i}}{\left(\sigma^2_{S2,-} + \sigma^2_{i,+}\right)^{1/2}}, \tag{13}$$

where $i =$ NE, C, or S3. This gives $Z_{NE} = 5.4$, $Z_C = 4.8$, and $Z_{S3} = 5.6$. Thus, the higher clump-opacity scale of S2 is separated from the values of the other three components at approximately 4.8σ–5.6σ under this one-parameter comparison. This statistic summarizes the marginal ν_{cl} constraints and is not intended to replace a full joint or hierarchical model comparison.

All components are dominated by steep, optically thin synchrotron emission. The SEDs differ primarily in the strength of low-frequency absorption and the location of the high-frequency cut-off. NE, C, and S3 have broadly comparable clump-opacity scales and covering factors within their uncertainties. C is distinguished by its detected diffuse component, whereas S2 is the clear outlier, with both a substantially higher ν_{cl} and a larger f_{cov}.

5 DISCUSSION

5.1 Synchrotron emission and model-selected free–free absorption

The cm–sub-mm SEDs of all four compact jet components are dominated by optically thin synchrotron emission, with $\alpha_{sy} \simeq -0.9$ to -1.7. NE and S3 have $\alpha_{sy} = -1.27^{+0.09}_{-0.09}$ and $-0.95^{+0.13}_{-0.17}$, respectively, C has $-0.94^{+0.13}_{-0.10}$, and S2 is steepest at $-1.67^{+0.14}_{-0.14}$. These values support the established non-thermal jet interpretation of the sub-arcsecond structure in NGC 1068 (T. W. B. Muxlow et al. 1996; J. F. Gallimore et al. 1996a, 2004; I. M. Mutie et al. 2024). The steep spectrum of S2 suggests stronger cooling or less efficient re-acceleration, whereas the flatter spectrum of C may reflect younger plasma, shocks, or unresolved flatter-spectrum structure (N. S. Kardashev 1962; R. D. Blandford & A. Königl 1979; C. L. Carilli et al. 1991).

The lowest measured synchrotron cut-off occurs in C, $\nu_c = 420^{+146}_{-103}$ GHz. NE and S3 have cut-offs of 634^{+244}_{-225} and 598^{+264}_{-231} GHz, respectively. For S2, the posterior does not localize the cut-off and only the lower limit $\nu_c > 418$ GHz can be reported.

The lower cut-off in C may indicate enhanced radiative losses or lower maximum electron energies near the nucleus (A. A. Rahman, S. Sahayanathan & P. A. Subha 2022; T. Chand & M. Böttcher 2024).

The model comparison in Section 4.1 shows that foreground ionized absorption is the principal source of spectral diversity. FFA is well established in NGC 1068 and is associated with ionized circumnuclear and disc/torus material (S. García-Burillo et al. 2014; C. Ramos Almeida & C. Ricci 2017; S. García-Burillo et al. 2019). NE shows the weakest absorption, with low diffuse opacity and $f_{cov} \sim 0.5$, consistent with a relatively unobscured near-side sightline (A. J. Young, A. S. Wilson & P. L. Shopbell 2001). S3 is intermediate, with $f_{cov} \sim 0.45$ and weak diffuse absorption.

C and S2 show stronger but distinct absorption. C has a measured diffuse component, $\nu_{diff} \simeq 2.1$ GHz, implying an extended ionized column in addition to partial-covering absorption (S. García-Burillo et al. 2024; C. Marconcini et al. 2025). S2 has the largest covering factor, $f_{cov} \sim 0.8$, and highest clump turnover frequency, $\nu_{cl} \simeq 26$ GHz, favouring compact, high-emission-measure ionized structures in a multiphase circumnuclear medium (S. García-Burillo et al. 2019; M. Revalski et al. 2021; J. Shin et al. 2021). This cannot be explained by leakage from S1: the pair is separated by 0.119 arcsec, or 1.99 common beams, their fitted amplitude correlation is only $|\rho| = 0.032$, and the conservative perturbation test gives $|\Delta\nu_{cl}| \lesssim 1.6$ GHz or $|\Delta f_{cov}| \lesssim 0.06$.

Components NE, C, and S3 have broadly comparable clump-opacity scales and covering factors within their uncertainties, consistent with the southern components being viewed through thicker, more inhomogeneous ionized material (e.g. S. García-Burillo et al. 2014; V. Gámez Rosas & others 2025). C's diffuse absorption further supports an extended nuclear ionized phase (e.g. J. F. Gallimore et al. 1996b, 2004; S. García-Burillo et al. 2021, 2024). The resolved SEDs therefore favour intrinsically synchrotron-dominated jet components whose observed differences are governed mainly by the structure and covering of foreground ionized gas. Variations in α_{sy} and ν_c may additionally trace differences in synchrotron ageing and particle acceleration.

Although this study does not measure feedback energetics directly, it identifies parsec-scale ionized structures that shape, and may respond to, the compact jet. The dense environment inferred towards C may also be relevant to hadronic interaction models for NGC 1068 (M. Aartsen et al. 2020; K. Fang et al. 2023), although this lies beyond the scope of this work.

5.2 Physical implications of the preferred clumpy absorber

The model comparison in Section 4.1 favours the partial-covering model over the diffuse-only alternative. We therefore examine

Downloaded from academic.oup.com/mnras/article/552/1/stag1693/8802537 by guest on 28 September 2026

what the fitted $f_{\rm cov}$ and $\nu_{\rm cl}$ values imply for the ionized material along the four sightlines.

The covering factors for NE, C, and S3 are

$$f_{\rm cov} = 0.53^{+0.08}_{-0.09}, \quad 0.43^{+0.10}_{-0.14}, \quad \text{and} \quad 0.46^{+0.12}_{-0.14},$$

with $\nu_{\rm cl} = 12.1^{+1.5}_{-1.4}$, $11.6^{+2.1}_{-2.2}$, and $11.0^{+1.7}_{-1.7}$ GHz, respectively. These similar values imply comparable FF opacities, but not identical absorber locations or structures. NE and S3 have only upper limits of $\nu_{\rm diff} < 1.59$ and < 1.56 GHz, whereas C has $\nu_{\rm diff} = 2.11^{+0.42}_{-0.25}$ GHz, supporting a patchy, multiphase medium rather than a simple radial opacity gradient.

Using the standard FF opacity approximation (e.g. A. Y. Yang et al. 2021),

$$\left(\frac{\nu_{\rm cl}}{\rm GHz}\right)^{2.1} = 3.28 \times 10^{-7} \left(\frac{T_{\rm e}}{10^4\,\rm K}\right)^{-1.35} \left(\frac{n_{\rm e}}{\rm cm^{-3}}\right)^{2} \left(\frac{D}{\rm pc}\right), \quad (14)$$

where $n_{\rm e}$ is the electron density and D the line-of-sight depth. Since $\rm EM = n_e^2 D$, adopting $T_{\rm e} = 10^4$ K gives

$$\left(\frac{n_{\rm e}}{\rm cm^{-3}}\right)^{2} \left(\frac{D}{\rm pc}\right) = 1.65 \times 10^{9} \left(\frac{\nu_{\rm cl}}{20\,\rm GHz}\right)^{2.1}. \quad (15)$$

This constrains the emission measure, but not the density, path length, filling factor, or location independently.

5.2.1 *The case for component NE*

Component NE lies substantially farther from S1 than C and S2, at a projected separation of approximately 0.65 arcsec, or ∼45 pc at the adopted distance of 14.4 Mpc. Its fitted $\nu_{\rm cl} = 12.1^{+1.5}_{-1.4}$ GHz should therefore not automatically be associated with compact torus material. For $T_{\rm e} = 10^4$ K, equation (15) gives

$$\rm EM_{NE} = \left(5.7^{+1.6}_{-1.3}\right) \times 10^{8}\ cm^{-6}\ pc,$$

or

$$D_{\rm NE} \simeq 5.7 \left(\frac{n_{\rm e}}{10^4\,\rm cm^{-3}}\right)^{-2} \rm pc.$$

Thus, $n_{\rm e} = 3 \times 10^4$ and $10^5\,\rm cm^{-3}$ correspond to characteristic depths of approximately 0.64 and 0.057 pc, respectively. The required emission measure can therefore arise in a pc or sub-pc-scale ionized cloud, a shock-compressed cloud surface, or foreground narrow-line-region material, without requiring torus clumps at the projected position of NE.

The moderate covering factor, $f_{\rm cov} = 0.53^{+0.08}_{-0.09}$, and weak diffuse-opacity constraint, $\nu_{\rm diff} < 1.59$ GHz, further show that only a subset of sightlines needs to intersect high-emission-measure gas. Previous radio imaging indicates that the north-eastern jet propagates through a dense and disturbed circumnuclear medium (J. F. Gallimore et al. 2004; I. M. Mutie et al. 2024), making a local jet–cloud interaction physically plausible. The present unresolved SED cannot distinguish such an interface from foreground narrow-line region (NLR) absorption; we therefore interpret the NE curvature as evidence for a partial-covering, high-emission-measure screen rather than direct evidence for torus clumps.

5.2.2 *The case for component S2*

Component S2 has the highest clump optical-depth scale, $\nu_{\rm cl} = 26.0^{+1.8}_{-2.1}$ GHz, and the largest covering factor, $f_{\rm cov} = 0.83^{+0.05}_{-0.07}$, indicating that most of its intrinsic synchrotron emission is intercepted by ionized gas. For $T_{\rm e} = 10^4$ K, equation (15) gives

$$\rm EM_{S2} = \left(2.86^{+0.43}_{-0.46}\right) \times 10^{9}\ cm^{-6}\ pc,$$

and hence

$$D_{\rm S2} \simeq 28.6 \left(\frac{n_{\rm e}}{10^4\,\rm cm^{-3}}\right)^{-2} \rm pc.$$

Confining the absorber to $D \lesssim 1$ pc requires $n_{\rm e} \gtrsim 5.3 \times 10^4\,\rm cm^{-3}$, while $D \simeq 0.1$ pc requires $n_{\rm e} \simeq 1.7 \times 10^5\,\rm cm^{-3}$. S2 therefore requires a substantially denser and more strongly covering absorber than NE, C or S3.

This interpretation is consistent with the projected location of S2, approximately 10 pc from the nucleus (I. M. Mutie et al. 2024), near the torus–inner NLR interface. The Compton-thick molecular torus extends over several parsecs (N. López-Gonzaga et al. 2014; F. E. Bauer et al. 2015; S. García-Burillo et al. 2016), while clumpy torus models permit strong sub-pc density contrasts and dense ionized cloud surfaces (M. Nenkova et al. 2008). Such structures can provide the required emission measure, although a contribution from dense inner-NLR gas cannot be excluded. As quantified in Section 4.3, the fitted $\nu_{\rm cl}$ of S2 is separated from those of NE, C, and S3 by approximately 4.8–5.6σ, confirming that its higher opacity scale is not merely a consequence of overlapping statistical uncertainties.

5.2.3 *Variability of the jet components*

Because the SEDs combine non-simultaneous observations, variability may broaden the inferred absorption parameters. An order-of-magnitude estimate can be obtained from equation (7): at $\nu = \nu_{\rm cl}$, where $\tau_{\rm cl} = 1$, the fitted covering factors imply synchrotron suppression of approximately 27 per cent–52 per cent across the four components. Propagating the quoted uncertainties in $f_{\rm cov}$ and $\nu_{\rm cl}$ indicates that inter-epoch flux-density changes of order 7 per cent–12 per cent could shift these parameters by roughly one statistical standard deviation. Variability at the ∼10 per cent level may therefore contribute appreciably to their uncertainties, particularly for C, where long-term changes have been reported (J. F. Gallimore et al. 2004; I. M. Mutie et al. 2024). However, reproducing the full absorption curvature without a foreground screen would generally require coherent frequency-dependent changes of several tens of per cent; for NE, the required offset is approximately 30 per cent–50 per cent around the turnover and approaches a factor of 2 at 5–7 GHz. We therefore regard variability as a secondary source of uncertainty rather than the primary origin of the fitted low-frequency curvature.

5.3 Physical interpretation synthesis: what sets the component-to-component SED diversity?

Taken together, the fitted parameters suggest a two-level interpretation. First, all four components are intrinsically synchrotron-dominated jet features with steep, non-thermal spectra, implying aged or continuously cooling electron populations. Secondly, the main driver of their observed spectral differences is not a large intrinsic change in synchrotron shape, but plausibly the differing structure and covering of foreground ionized gas. In this picture, NE traces a relatively clear sightline, S3 an intermediate one, C probes both clumpy and diffuse nuclear ionized gas, and S2 intersects the densest and most

Downloaded from academic.oup.com/mnras/article/552/1/stag1693/8802537 by guest on 28 September 2026

compact absorber population, plausibly near the torus–inner NLR interface.

6 SUMMARY AND CONCLUSIONS

We present parsec-scale cm-to-sub-mm SEDs of the compact jet components NE, C, S2, and S3 in NGC 1068 using matched-*uv* *e*-MERLIN, VLA, and ALMA data spanning 4.5–706 GHz at a common 0.06 arcsec (∼4 pc) resolution. Spatial-deblending tests show that inter-component contamination is small. Even for the closest pair, S1–S2, neighbour perturbations change the recovered flux by less than 1 per cent, while the largest injection–recovery error is 3.07 per cent. A conservative centroid shift gives $|\Delta\nu_{\rm cl}| \lesssim 1.6$ GHz or $|\Delta f_{\rm cov}| \lesssim 0.06$ for S2, insufficient to explain its distinct absorption signature.

Confirming their non-thermal jet origin, all four components are dominated by steep, optically thin synchrotron emission with spectral indices ranging from $\alpha_{\rm sy} \simeq -0.9$ to -1.7. The spectral cut-off $\nu_{\rm c}$ is measured at approximately 420 GHz in component C and 600–630 GHz in components NE and S3; for S2, only a lower limit of $\nu_{\rm c} > 418$ GHz can be established. This variance points to localized changes in radiative losses or maximum electron energies along the inner jet.

Foreground ionized absorption is the principal source of spectral diversity. AIC and BIC comparisons favour the partial-covering absorber, most strongly for S2. NE and S3 show moderate covering factors and turnovers near 11–12 GHz, while C requires both partial-covering and diffuse absorption. S2 is the most absorbed component, with $f_{\rm cov} = 0.83^{+0.05}_{-0.07}$ and $\nu_{\rm cl} \simeq 26$ GHz, consistent with a dense, high-emission-measure screen near the torus–inner-NLR interface. The clump-opacity scale of S2 differs from those of NE, C, and S3 at approximately 4.8–5.6σ in a conservative Gaussian-equivalent comparison.

No off-nuclear component requires a statistically significant mm–sub-mm excess above the synchrotron model. The observed SED differences therefore arise mainly from variations in the structure and covering of foreground ionized gas, rather than fundamentally different intrinsic emission mechanisms.

Future high-resolution observations below ∼4 GHz will be essential for constraining the turnover shape and separating covering factor, density, and path-length effects in the absorbing medium.

ACKNOWLEDGEMENTS

We thank Development in Africa with Radio Astronomy (DARA, Phase 3) for funding this research through the UK's Science and Technologies Facilities Council (STFC) grant ST/Y006100/1. We thank *e*-MERLIN, the VLA, and the ALMA for the observations. *e*-MERLIN is a National Facility operated by the University of Manchester at Jodrell Bank Observatory on behalf of STFC. The VLA is operated by the National Radio Astronomy Observatory (NRAO). The NRAO is a facility of the National Science Foundation, operated under a cooperative agreement by Associated Universities, Inc. ALMA data are used by ADS/JAO.ALMA #: 2013.1.00055.S, 2016.1.00232.S, 2017.1.01666.S, 2018.A.00038.S, and 2021.1.00279.S. ALMA is a partnership of ESO (representing its member states), NSF (USA), and NINS (Japan), together with NRC (Canada), NSTC, and ASIAA (Taiwan), and KASI (Republic of Korea), in cooperation with the Republic of Chile. The Joint ALMA Observatory is operated by ESO, AUI/NRAO, and NAOJ. We acknowledge support from the UK SKA Regional Centre (UKSRC). The UKSRC is a collaboration between the University of Cambridge, University of Edinburgh, Durham University, University of Hertfordshire, University of Manchester, University College London, and the UKRI STFC Scientific Computing at RAL. The UKSRC is supported by funding from the UKRI STFC. SdP and SA acknowledge support from ERC Advanced Grant 789410.

DATA AVAILABILITY

The data on which this paper is based are publicly available from the *e*-MERLIN, VLA, and ALMA archives under projects IDs described in table 1 of I. M. Mutie et al. (2025). Calibrated image products are available upon reasonable request to the corresponding author.

REFERENCES

Aartsen M. et al., 2020, Phys. Rev. Lett., 124 051103
Ashton G. et al., 2019, ApJS, 241, 27
Bauer F. E. et al., 2015, ApJ, 812, 116
Blandford R. D., Königl A., 1979, ApJ, 232, 34
Carilli C. L., Perley R. A., Dreher J. W., Leahy J. P., 1991, ApJ, 383, 554
Chand T., Böttcher M., 2024, ApJ, 962, 31
Clemens M. S., Scaife A., Vega O., Bressan A., 2010, MNRAS, 405, 887
Conway J. E., Elitzur M., Parra R., 2018, ApJ, 865, 70
del Palacio S. et al., 2025, A&A, 701, A41
Fang K., Rodriguez E. L., Halzen F., Gallagher J. S., 2023, ApJ, 956, 8
Foreman-Mackey D., Hogg D. W., Lang D., Goodman J., 2013, PASP, 125, 306
Gallimore J. F., Baum S. A., O'Dea C. P., Pedlar A., 1996a, ApJ, 458, 136
Gallimore J. F., Baum S. A., O'Dea C. P., Brinks E., Pedlar A., 1996b, ApJ, 462, 740
Gallimore J. F., Baum S. A., O'Dea C. P., 2004, ApJ, 613, 794
Gámez Rosas V. et al., 2025, A&A, 699, A187
García-Burillo S. et al., 2014, A&A, 567, A125
García-Burillo S. et al., 2016, ApJ, 823, L12
García-Burillo S. et al., 2019, A&A, 632, A61
García-Burillo S. et al., 2021, A&A, 652, A98
García-Burillo S. et al., 2024, A&A, 689, A347
Impellizzeri C. M. V. et al., 2019, ApJ, 884, L28
Järvelä E., Berton M., Crepaldi L., 2021, Front. Astron. Space Sci., 8, 147
Kardashev N. S., 1962, Sov. Astron., 6, 317
Lacki B. C., 2013a, in Torres D. F., Reimer O. eds, Astrophysics and Space Science Proceedings, Vol. 34, Cosmic Rays in Star-Forming Environments. p. 411
Lacki B. C., 2013b, MNRAS, 431, 3003
López-Gonzaga N., Jaffe W., Burtscher L., Tristram K. R. W., Meisenheimer K., 2014, A&A, 565, A71
Marconcini C. et al., 2025, preprint (arXiv:2512.11042)
McMullin J. P., Waters B., Schiebel D., Young W., Golap K., 2007, in Shaw R. A., Hill F., Bell D. J., eds, ASP Conf. Ser., Vol. 376, Astronomical Data Analysis Software and Systems XVI. Astron. Soc. Pac., San Francisco , p. 127
Mutie I. M. et al., 2024, MNRAS, 527, 11756
Mutie I. M., del Palacio S., Beswick R. J., Williams-Baldwin D., Gallimore J. F., Gallagher J. S., Aalto S. E., Baki P. O., 2025, MNRAS, 539, 808
Muxlow T. W. B., Pedlar A., Holloway A. J., Gallimore J. F., Antonucci R. R. J., 1996, MNRAS, 278, 854

Downloaded from academic.oup.com/mnras/article/552/1/stag1693/8802537 by guest on 28 September 2026

Nenkova M., Sirocky M. M., Nikutta R., Ivezić Ž., Elitzur M., 2008, ApJ, 685, 147
Rahman A. A., Sahayanathan S., Subha P. A., 2022, MNRAS, 515, 1410
Ramírez-Olivencia N., Varenius E., Pérez-Torres M., Alberdi A., Conway J. E., Alonso-Herrero A., Pereira-Santaella M., Herrero-Illana R., 2022, A&A, 658, A4
Ramos Almeida C., Ricci C., 2017, Nat. Astron., 1, 679
Revalski M. et al., 2021, ApJ, 910, 139
Shin J., Woo J.-H., Kim M., Wang J., 2021, ApJ, 908, 81
Viti S. et al., 2014, A&A, 570, A28
Yang A. Y. et al., 2021, A&A, 645, A110
Young A. J., Wilson A. S., Shopbell P. L., 2001, ApJ, 556, 6

SUPPLEMENTARY MATERIAL

Supplementary data are available at *MNRAS* online.

SED_NGC_1068_Jet_Components_Supplementary Materials_final

Please note: Oxford University Press is not responsible for the content or functionality of any supporting materials supplied by the authors. Any queries (other than missing material) should be directed to the corresponding author for the article.

This paper has been typeset from a TEX/LATEX file prepared by the author.

Downloaded from academic.oup.com/mnras/article/552/1/stag1693/8802537 by guest on 28 September 2026

© The Author(s) 2026.
Published by Oxford University Press on behalf of Royal Astronomical Society. This is an Open Access article distributed under the terms of the Creative Commons Attribution License (https://creativecommons.org/licenses/by/4.0/), which permits unrestricted reuse, distribution, and reproduction in any medium, provided the original work is properly cited.